



PCCP

Analysis of an All-Solid State Nanobattery using Molecular Dynamics Simulations Under an External Electric Field

Journal:	<i>Physical Chemistry Chemical Physics</i>
Manuscript ID	CP-ART-05-2020-002851.R4
Article Type:	Paper
Date Submitted by the Author:	13-Nov-2020
Complete List of Authors:	Ponce, Victor; Texas A&M University System, Electrical Engineering & Chemical Engineering Galvez-Aranda, Diego; Texas A&M University College Station, Electrical and Computer Engineering Seminario, Jorge; Texas A&M University College Station,

SCHOLARONE™
Manuscripts

Analysis of an All-Solid State Nanobattery using Molecular Dynamics Simulations Under an External Electric Field

Victor Ponce^{1,2} Diego E. Galvez-Aranda,^{1,3} and Jorge M. Seminario^{1,2,3,*}

¹Department of Chemical Engineering

²Department of Materials Science and Engineering

³Department of Electrical and Computer Engineering

Texas A&M University

College Station, TX 77843, USA

ABSTRACT

Present Li-ion batteries (LIB) technology require strong improvements in performance, energy capacity, charging-time, and cost to expand their application to e-mobility and grid storage. Li-metal is one of the most promising materials to replace commercial anodes such as graphite because of its 10 times higher specific capacity. However, Li-metal has high reactivity with commercial liquid electrolytes; thus, new solid materials are proposed to replace liquid electrolytes when Li-metal anodes are used. We present a theoretical analysis of the charging process in a full nanobattery, containing a LiCoO_2 cathode, a $\text{Li}_7\text{P}_2\text{S}_8\text{I}$ solid-state electrolyte (SSE), a Li-metal anode as well as Al and Cu collectors for the cathode and anode, respectively. In addition, we added a $\text{Li}_3\text{P}/\text{Li}_2\text{S}$ film as solid electrolyte interphase (SEI) layer between the Li-anode and SSE. Thus, we focus this study on the SEI and SSE. We simulated the charging of the nanobattery with an external voltage by applying an electric field. We estimated temperature profiles within the nanobattery and analyzed Li-ion transport through the SSE and SEI. We observed a slight temperature rise at the SEI due to reactions forming PS_3^- and $\text{P}_2\text{S}_7^{4-}$ fragments at the interfaces; however, this temperature profile changes due to the charging current under the presence of the external electric field $\mathcal{E} = 0.75 \text{ V/\AA}$. Without the external field, the calculated open-circuit voltage (OCV) was 3.86 V for the battery, which is within the range of values of commercial cobalt-based LIBs. This voltage implies a spontaneous fall of available Li-ions from the anode to the cathode (during discharge). The charge of this nanobattery requires overcoming the OCV plus an additional voltage that determines the charging current. Thus, we applied an external potential able to neutralize the OCV, plus an additional 1.6 V to induce the transport of Li^+ from the cathode up to the anode. Several interesting details about Li^+ transport paths through the SSE and SEI are discussed.

*Corresponding author: seminario@tamu.edu, Telephone: (979) 845-3301

INTRODUCTION

Research on solid-state electrolytes (SSEs) started more than 200 years ago with Faraday's work using Ag_2S and PbF_2 .¹ Nowadays, decarbonization is growing to eliminate carbon fuels effects in global warming in favor of renewable energies such as solar and wind energies, for which energy storage will play an important role.² Li-ion batteries are ubiquitous in portable devices; however, their proliferation in e-mobility and grid storage, require strong improvements in performance, energy capacity, charging-time, and cost that cannot be satisfied with present Li-ion batteries (LIB). Thus, recently, SSEs have been proposed as safe materials against Li-metal anodes typical

problems such as dendrite growing^{3,4} and low energy-densities.⁵ In addition, SSEs have much less irreversible capacity losses than liquid electrolytes when using an NMC cathode; the capacity retention is 90.6% after 10,000 cycles;⁶ and SSEs optimize packaging and stacking as well as increases energy density better than commercial liquid electrolytes such as organic and acid-based electrolytes.⁷ On the other hand, atomistic computational chemistry techniques such as quantum and classical molecular dynamics are tools that become complementary to experimental techniques, helping us to understand how the chemistry works, characterizing new compounds and materials, and processing large amounts of data from the simulations to integrate chemical theory and modeling with experimental observations. Recently, we introduced the concept of a nanobattery,^{8,9} which, complemented with earlier work, has become our testbed for the testing of proposed materials for several parts of a battery.¹⁰⁻¹⁶

In the present work, we aim to understand the atomistic behavior involving reactions, temperature profiles, drifts paths, and external electric field effects simulating the charging through molecular dynamics simulations on a full nanobattery with Li-metal anode, solid-state electrolyte $\text{Li}_7\text{P}_2\text{S}_8\text{I}$, and LiCoO_2 cathode, in addition to the usual current collectors of aluminum and copper for the cathode and anode, respectively. Since lithium-metal always presents an undefined native film covering its surface such as Li_2O accompanied by LiOH and Li_2CO_3 ,¹⁷⁻²⁵ it is a good practice to pretreat the native film-free Li metal surface with suitable added films. In this case we have chosen a double layer $\text{Li}_3\text{P}/\text{Li}_2\text{S}$, which is consistent and compatible with the solid electrolyte $\text{Li}_7\text{P}_2\text{S}_8\text{I}$, since both Li_3P and Li_2S are products of decomposition of sulfide electrolytes on the Li-metal anode surface.²⁶ In addition, Li_2S improves the ionic conductivity and suppresses the Li dendrite growth of Li-metal anodes²⁷ and Li_3P suppresses formation of dendrites and enhances the Li diffusion at the interphase SEI-anode.²⁸ Li_3P and Li_2S were also reported as SEI in experiments using $\text{Li}_7\text{P}_2\text{S}_8\text{I}$ in a graphite battery.²⁹ We observe a Li^+ hopping diffusion mechanism similar to one in $\text{Li}_7\text{P}_2\text{S}_8\text{I}$ reported by Kang et al.³⁰ and to one in $\text{Li}_{10}\text{GeP}_2\text{S}_{12}$.³¹ Finally, our results are also in agreement with a report that found that Li^+ ionic conductivity in sulfide-based SSE depends on the distribution of PS_4 tetrahedrons, which form the Li^+ diffusion channel.³²

NANOBATTERY DESCRIPTION AND METHODOLOGY

We perform classical molecular dynamics (MD)³³ simulations using the Large-scale Atomic/Molecular Massively Parallel Simulation (LAMMPS) program.³⁴ Initial geometry of simulated full cell (Figure 1) contains from right to left, Al current collector, LiCoO_2 cathode, $\text{Li}_7\text{P}_2\text{S}_8\text{I}$ solid state electrolyte, $\text{Li}_3\text{P}/\text{Li}_2\text{S}$ added SEI films, Li-metal anode, and Cu current collector. Although the dimensions of our atomistic-based nanobattery model are roughly three orders of magnitude smaller than those of commercial batteries,³⁵ nevertheless most of the interesting chemistry is local; thus having represented few shells of nearest neighbor atoms around them plus the use periodic boundary conditions may strongly alleviate this issue and provide interesting insights.

Visualization of trajectories and post-processing analyses are performed with the programs, Visualization Molecular Dynamics (VMD)³⁶ and the open visualization tool (OVITO).³⁷ Periodic boundary conditions (PBC) were applied in the three directions; however, in the longitudinal direction, we set the current collectors (Al and Cu) parameters such that they eliminate the interaction of the anode-cathode due to the PBC. Force fields parameters are shown in Table 1. We used a reactive force field for S, P, Li^+ and Li-metal in the SEI and anode developed by Islam

et al.³⁸ A Morse potential is used for the pair interactions P-S and P-I in the SSE: $E(r) = D_0(e^{-2\alpha(r-r_0)} - 2e^{-\alpha(r-r_0)})$; D_0 = dissociation energy, r_0 = equilibrium distance, and α = width parameter, $\alpha = \sqrt{k/D_0}$, k = force constant. P-S parameters D_0 , r_0 and k are 1.58 eV, 2.1 Å and 12.2 eV/Å², respectively.

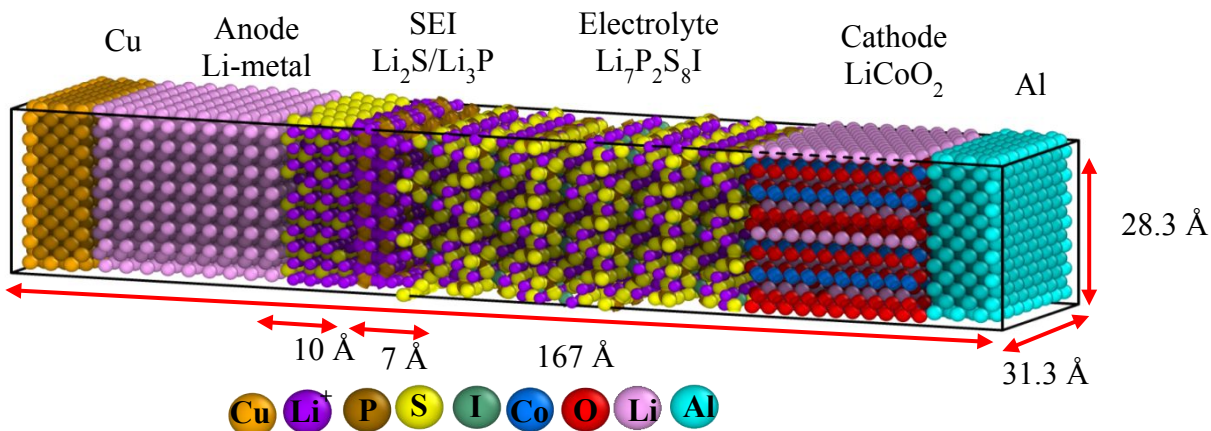


Figure 1. Initial geometry of the full nanobattery. From left to right, Cu current collector, Li-metal anode, Li₂S/Li₃P SEI films, Li₇P₂S₈I solid-state electrolyte, LiCoO₂ cathode, and Al current collector. The current collectors are Cu₈₆₄ and Al₆₇₂, the anode is Li₁₂₉₆, SEI are (Li₂S)₂₂₆ and (Li₃P)₁₁₂, SSE is (Li₇P₂S₈I)₁₂₀, cathode is (LiCoO₂)₇₅₆; the total number of atoms in the simulation box is 9,142

P-I parameters for D_0 , r_0 and k are 1.82 eV, 2.5 Å and 9.3 eV/Å², respectively. P-S and P-I interactions were calculated from the B3PW91³⁹⁻⁴¹/cc-pVTZ(P,S)⁴²⁻⁴⁴/LANL2DZ(I)⁴⁵⁻⁴⁸ level of theory using the program Gaussian-16.⁴⁹ First we fully optimized PS₃I and PS₄, which were started with tetrahedral geometries;⁵⁰ then, we stretched the P-I and one P-S bonds, respectively, performing partial optimizations at every point of the potential surface. The threshold for the force was set to 2.5×10^{-7} kcal mol⁻¹ Å⁻¹. For the interactions at the cathode we use a force field developed in the past for a full Li-ion nanobattery.⁸ The cathode is modeled with harmonic bond and angle potentials $E_b = k_b (r - r_0)^2$ and $E_a = k_a (\theta - \theta_0)^2$, respectively, where $k_b = 40$ kcal/molÅ², $k_a = 139.4$ kcal/mol(radian)², $r_0 = 1.92$ Å, and $\theta_0 = 90^\circ$. The current collectors are modeled as inert hypothetical material with a non-reactive Lennard-Jones potential, $\epsilon = 2.5$ kcal/mol and $\sigma = 2.3$ Å for Cu, and $\epsilon = 1.0$ kcal/mol and $\sigma = 2.5$ Å for Al. These current collectors also avoid the shifting of atoms due to the periodicity along the longitudinal direction. Cu and Al are set with a weak attractive component using a Lennard-Jones potential with $\epsilon = 0.01$ kcal/mol and $\sigma = 2.4$ Å. Specific effects of the current collectors are not being studied this time. All Coulombic charges used in the simulations were the formal charges of 1, 5, -3, -2, and -1 for Li(Li₇P₂S₈I), P(Li₇P₂S₈I), P(Li₃P), S(Li₇P₂S₈I/Li₂S), and I(Li₇P₂S₈I), respectively. All other atom charges were set to zero.

We optimize the initial geometry shown in Figure 1 using the Polak-Ribiere algorithm⁵¹ with a force convergence criterion on each atom of 10^{-8} kcal mol⁻¹ Å⁻¹ to fix any unusual bond created initially by setting all components. Then, we run MD equilibration steps at 5 K for 200 ps with a time step 0.1 fs under the NPT ensemble⁵² to eliminate any remaining hot spots in the initial geometry. This is followed by a temperature increase from 5 to 300 K for 200 ps, i.e., with a

heating rate of 1.48 K ps⁻¹ under the NPT ensemble. Finally, another equilibration under NPT ensemble for 200 ps (Figure 2). We use the Nose–Hoover thermostat⁵³ with a damping parameter of 50 fs. This procedure should be sufficient to obtain an equilibrated system as corroborated in Figure 2.

Table 1. Force field parameters used in this work. ReaxFF are from Reference;³⁸ we adopted them with formal charges because they are well-suited to represent intermolecular effects.¹⁰ The other parameters were calculated from DFT geometry optimizations and second derivative calculations at the local minima.

Species	Type	D_0 (eV)	r_0/σ (Å)	k (eV/Å ²)	q (e)
P(SSE)	ReaxFF ³⁸				5
P(SEI)	ReaxFF ³⁸				3
S	ReaxFF ³⁸				-2
I	ReaxFF ³⁸				1
Li	ReaxFF ³⁸				-1
P-I	Morse	1.82	2.5	9.3	
P-S	Morse	1.58	2.1	12.2	
Co	L-J	0.008		3.4	0
O	L-J	0.026		2.8	0
Co-O	Harmonic		1.92	1.73	
Cu	L-J	0.1	2.3		0
Al	L-J	0.043	2.5		0
Al-Cu	L-J	0.0004	2.4		

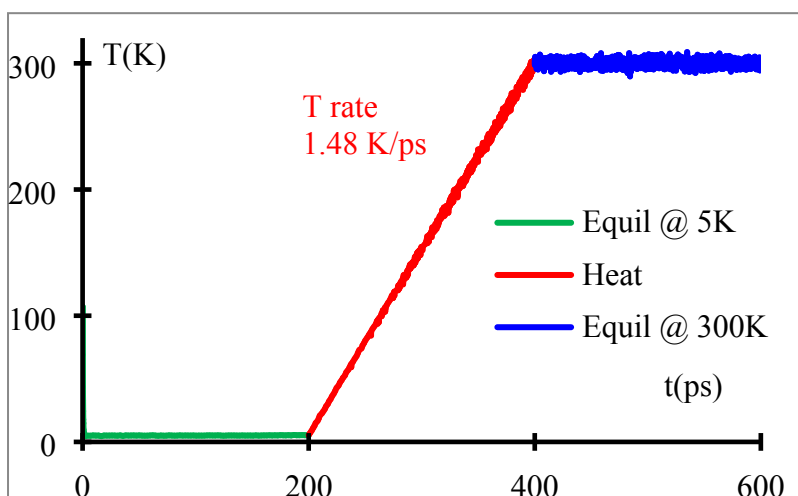


Figure 2. Temperature evolution of the SSE nanobattery

In order to set an external pressure and temperature to our system, the NPT ensemble with the Nose-Hoover thermostat⁵⁴ described by Melchionna et al.⁵⁵ is used as implemented in the program LAMMPS.³⁴ Thus, to set the system at temperature T_{ext} (e.g., 300K) and pressure P_{ext} (e.g., 1 atm) the system (box) should be under a bath of temperature T_{ext} and an external pressure P_{ext} performed by a piston with a pseudo mass W ; therefore, the equations of motion ($\ddot{x}_i = F/m_i$) are modified to

$$\dot{v}_i(t) = \frac{F_i(t)}{m_i} - \frac{v_T p_i(t)}{2m_i} - v_T^2 r_i(t) \left(\frac{T(t)}{T_{ext}} - 1 \right)$$

where,

$$v_i(t) = s \dot{r}_i(t)$$

$$s = e^{-v_T \Delta t / 2}$$

v_T = thermostetting rate (50 fs⁻¹)

Δt = time step (0.1 fs)

r_i = position of the atom i

$F_i(t)$ = resultant force in atom i

$p_i(t)$ = atomic momentum of atom i

then, the instantaneous temperature $T(t)$ and pressure $P(t)$ at time t are

$$T(t) = \sum_{i=1}^N \frac{m_i v_i^2(t)}{k_b N}$$

where,

m_i = mass of the atom i

v_i = velocity of the atom i at time t

k_b = Boltzmann constant

N = total number of atoms in the system.

On the other hand, the instantaneous $P(t)$,

$$P(t) = \frac{NRT(t)}{V(t)}$$

R = Gas constant

$V(t)$ = volume of the system at time t

Then, the volume is obtained from

$$\ddot{V} = -\frac{v_P}{2} \dot{V} + \frac{s^2}{W} \left(\frac{NRT(t)}{V} - P_{ext} \right)$$

where,

v_P = barosetting rate (100 fs⁻¹)

W = piston with a pseudo mass (20 amu Å⁻⁴)

Finally, the instantaneous kinetic energy is given by

$$E_k(t) = \frac{3}{2}k_B T(t)$$

RESULTS AND DISCUSSION

Temperature profiles of the nanobattery were calculated along the longitudinal axis from all atoms, except from those at the current collectors (Al, Cu), during the 50 ps after equilibration at 300K and during the next first 10 ps during the application of the external electric field (Figure 3) in longitudinal intervals of 4 Å, which was a good trade-off between resolution and fluctuations. We located a small temperature rise reaching ~315K in the SEI when no field was applied; this is, most likely, because the reactions taking place around the solid-state electrolyte. However, when the electric field was applied, we observe a larger temperature in the electrolyte (near the cathode). This is due to oxidizing reactions taking place at the electrolyte cathode interface and to less extent to the relatively higher Li-ion-resistance of the electrolyte with respect to the cathode. Kinetic energy from Li-ions is transferred as vibrational energy to the atoms in the electrolyte. After this mismatch of impedances (from cathode to electrolyte), the temperature decreases approaching the SEI, where again a small increase in temperature is observed as it took place without electric field, during the setting of the battery. The anode is warmer than the cathode and most of the electrolyte because of its metallic character. During the charging cycle the anode and cathode maintain roughly at the same temperature, but temperature is higher in the electrolyte due to its higher cationic resistance. Although the ionic conductivity of the SSE is $6.3 \times 10^{-4} \text{ S.cm}^{-1}$,⁵⁶ against the $3.4 \times 10^{-5} \text{ S.cm}^{-1}$ of the cathode,⁵⁷ still the resistance can be comparable due to the larger length of the electrolyte. On the other hand, having better electronic conductivity, both electrodes are better heat dissipators, able to maintain lower temperatures. Also, the SEI is a barrier to the thermal phonons from the metallic anode. Therefore, temperature increases in the SEI and SSE due to their larger ionic resistance with respect of the anode and cathode;

Under the above conditions, what we obtain is the end of a transient-state of the battery at a global stable temperature of 300K (Figure 2); this state is characterized by a steady-state temperature with small fluctuations and a time-independent gradient in the different regions of the battery, typical of an open system as energy is inserted or subtracted to control the temperature or to drive the charging of the battery. Thus, the gradient of temperature is simply due to the different thermal behavior of the components of the battery in response to the external temperature bath or the external power source. Thus, the temperature profile shown in Figure 3 indicates that the anode and SEI are warmer than the electrolyte and cathode in the unbiased battery. Also shown is the temperature profile when the battery is biased to be charged. In this latter case, in addition to the thermostat, we have the external voltage source adding energy continuously to drive the Li-ions to the anode. Therefore, there is not thermal equilibrium as we are dealing with a nonequilibrium system. After a transient-state, the average temperature as a function of time reaches a constant value but it is not the same spatially. There are no changes of temperature locally as each point in space reaches a constant value, but the temperature as a function of the coordinates is different at each point, simply because their different response to the thermal and electrical inputs. During the transient state, the local temperatures raise until reaching a constant value. The number of products also reaches a constant value during the period from 400 to 600 ps (Figure 4) at 300K, thus the

unbiased battery reached its steady-state. Without external bias but with the heat controller, the metallic region of the battery shows higher temperatures than the ceramic oxide or ionic material of the cathode. Temperature slightly increases at the SEI interphase, which behaves like a barrier to thermal phonons from the metallic anode. The temperature decay in going from the SEI to the cathode because the cathode is an ionic material, the most stable in the battery or the one with the lowest energy but also with a higher heat capacity than the metallic anode; on the other hand, it is easier for the anode than the cathode to dissipate thermal energy because of the higher heat conductivity of the former. When an external source is applied to the battery, (to charge the battery). When the external bias is applied, the temperature increases in the cathode as Li from the cathode is oxidized and produce friction to leave the oxide. The temperature further increases in the electrolyte due to the resistance of the electrolyte, which is much longer than the length of cathode traveled by the Li-ion. The temperature decreases again in the anode due to the small resistance due to the short path traveled by the current of Li-ions. The product formations remain constant when the steady state at 300K is reached; and the product formations increase when the electric field is applied, which becomes a perturbation to the steady state. Before charging the battery, the cathode is less energetic for Li-ions than the anode is, thus the Li^+ prefers to stay in the cathode; during the battery charging, the cathode becomes more energetic than the anode due to the external bias, thus the Li^+ prefers to migrate to the anode. And, as we will see in the next section (Figure 5), our MD simulations suggest a battery open circuit voltage that is fully compatible with all commercial and experimental Li-ion batteries.

Although an SSE should be a good ion-conductor and poor electron conductor, the cathode should also be a good ion conductor as well as electron conductor. Thus, the cathode as a good ion conductor has not difference with the electrolyte except when the ion is reduced or neutralized in the cathode, moment at which the reduced Li (or Li-neutral, or Li and its closest neighborhood) is strongly bonded until it is oxidized again with a strong external field during the charge of the battery. The low ionic conductivity of the electrolyte is a limiting factor, among several perhaps equally or more important factors such as structural stability and formation of a benign solid electrolyte interphase. However, the SEI is usually of lower ionic conductivity than electrodes and electrolytes and is the place where most reactions take place when applying the external bias.

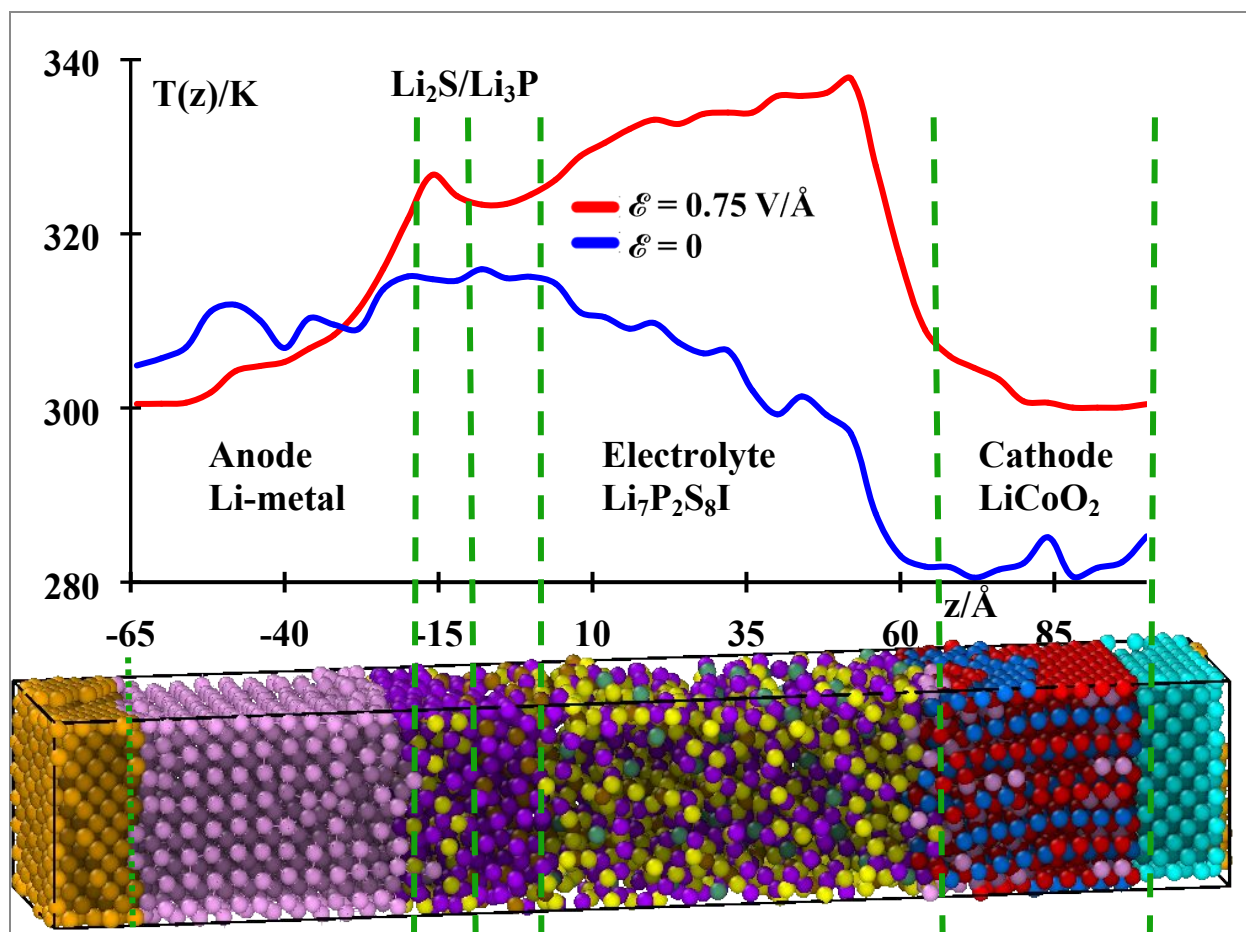


Figure 3. Average temperature profile of the SSE battery during the last 50 ps of MD simulations without electric field $\mathcal{E} = 0$ (blue) and during the first 10 ps under electric field, $\mathcal{E} = 0.75 \text{ V/\AA}$ (red). Both simulations were performed under NPT ensembles and each frame is taken every 100 fs. Temperature profiles were calculated in longitudinal slabs of 4 \AA each.

Perhaps the presence of temperature gradients before the application of the external electric field might bring some issues regarding the equipartition theorem. Since the thermostat only controls the kinetic energy of the whole system, our reported gradients are not the results of an equilibration, but they corresponded to the end of a transient state at the interfaces perhaps at odds with the equipartition theorem. However, a thermal equilibrium connected to the equipartition theorem is not applicable in some situations; therefore, a mathematical formalism was developed to adapt the equipartition theorem with quantum mechanics, see for instance, Dence.⁵⁸ Although most of the issues with the equipartition theorem are because the quantum nature of atomistic systems, classical MD calculations use powerful force fields with some theoretical and empirical information from their quantum character such as the effects of electrons and other quantum effects implicitly fitted in the force fields. Therefore, we expect to get realistic results from our simulations that go beyond the equipartition theorem, especially for solids forming interfaces and interphases, which by their solid nature avoid most of the diffusional equilibrium because most atoms from one type of solid do not travel to another different. Although the Nose-Hover algorithm has no preference for the energy exchange, still this is an input energy and the response of the different materials to such inputs can be totally different according to the nature of each

material (such as their heat capacity and conductivity). Formally speaking, the classical equipartition theorem can be used only if all vibrational modes are fully activated. However, this applies exactly only as the temperature goes to infinity.^{59,60} For finite temperatures, we can still come close if the thermal energy is high enough versus the energy required to excite the vibrational modes, i.e., $k_B T \gg \hbar\omega$. Although for most elements, room temperature is high enough to come close to full excitation; however, there are solids such as diamond, silicon, and germanium where room temperature is not enough to validate the equipartition theorem.⁶¹⁻⁶³

Speciation at the SEI: PS_3^- and $\text{P}_2\text{S}_7^{4-}$ (Figure 4) number of fragments (n) are formed at lithium-metal/SEI and SEI/SSE interfaces due the PS_4^{3-} and PS_3I^{2-} anions dissociation in the absence of an external electric field. PS_4^{3-} begins to dissociate at 300K in small amounts $n = \sim 3$, equivalent to only 1.6% of the total PS_4^{3-} . PS_3I^{2-} dissociates into 20 species almost instantly at 5K, forming PS_3^- and I^- . PS_4^{3-} reacts with PS_3^- , forming $\text{P}_2\text{S}_7^{4-}$ (Figure 4) under the presence of the external electric field, $\mathcal{E} = 0.75 \text{ V/\AA}$. All these species are recreating a new SEI. The $n(t)$'s are just counters; they count the number of species being formed or destroyed. Every 100 fs we count the number of species in the whole simulation box. The species are determined by checking all bonds against thresholds bond lengths. Thus, Figure 4 shows the evolution of the number of products when the interface is formed followed by those products when the battery is set to charge under an external power source. The speciation numbers, $n(t)$, provide important information regarding the initial composition of a solid electrolyte interface before the application of an external field and right after. A good design of a battery should have a prediction of what the SEI is going to be or if the SEI has the correct characteristics or not. Another direct implication of this plot is the reactive behavior of the Li-metal surface on the solid electrolyte $\text{Li}_7\text{P}_2\text{S}_8\text{I}$, and the native SEI artificially added, $\text{Li}_2\text{S}/\text{Li}_3\text{P}$, all of which decompose into components PS_4^{3-} and $\text{P}_2\text{S}_7^{4-}$ under the presence of the Li-metal surface. Such a reaction can be followed with the good resolution of molecular dynamics methods, providing further decomposition species.

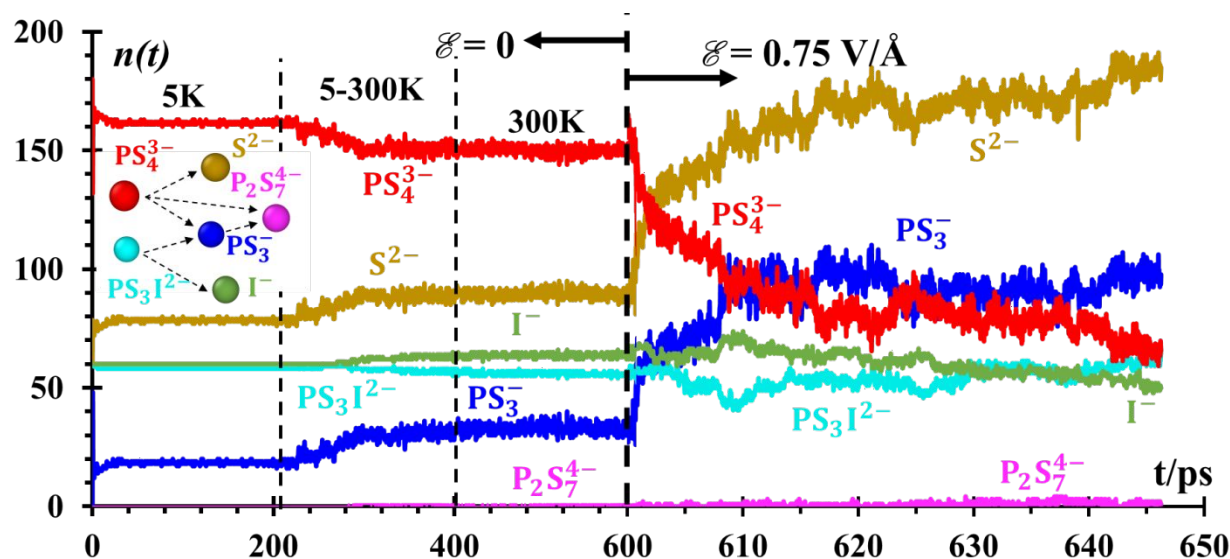


Figure 4. Speciation numbers, n , as functions of time, t , at the lithium-metal/SSE interface during all stages of the NPT MD simulations, including under the external electric field. The last 50 ps before the application of the electric field are the production runs without field. The time (t) scale in the graph is exploded when the electric field $\mathcal{E} = 0.75 \text{ V/\AA}$ is applied at 600 ps. The inset shows the most likely

reaction/degradation network about the SSE during the simulations. Speciation analyses were limited to the SEI and SSE, i.e., to species containing P, S, and I.

These speciation numbers explain experimental evidence and they are related to the transport of Li-ions. For example, they explain the formation of PS_3^- and $\text{P}_2\text{S}_7^{4-}$, which takes place before and after the charging. The speciation numbers also predict that the products formation remain constant before the electric field is applied and once it is applied, the product formations increase; there are experimental evidence for this:⁶⁴ The use of Li_2S in the artificial SEI for the nanobattery is supported by the formation of Li_2S at long times and the stabilization of the PS_3 and PS_4 anions in the SSE phase and interphase, changing the electronic and ionic properties of the SEI.⁶⁴ The Li_2S as SEI improves the ionic conductivity and suppresses the Li dendrite growth of Li metal anode.²⁷

External Electric Field Effect on the Battery Potentials: Average lithium potential energies (Figure 5) are calculated in longitudinal slabs of 0.5 Å width along the z-axis. For the curve before applying the external electric field (blue), we calculated the potential energy profile from the potential energy of each atom, we integrated the potential energy of each atom in the longitudinal direction (longitudinal slabs of 0.5 Å each) then we obtained the average of the potential profiles during the last 50 ps of the equilibration at 300K over 500 frames, each frame was taken every 100 fs. A similar approach was followed for the case with electric field applied to the nanobattery, except that the geometries are obtained from the MD with $\mathcal{E} = 0.75 \text{ V/\AA}$ applied and the average of the potential profiles were obtained during the first 10 ps of the application of $\mathcal{E} = 0.75 \text{ V/\AA}$ at 300K over 100 frames, each frame was taken every 100 fs. In order to simulate the charge of the battery under an external pressure and temperature, we continue using the NPT ensemble under the external electric field as relaxation of the volume during the charging is important to determine the stability of the interphase.

Even though, canonical ensembles might present problems to calculate dynamical properties at equilibrium and nonequilibrium conditions because thermostat interference and other approximations, canonical ensembles still can reach equivalent results to those from microcanonical ensembles.^{65,66} For example, an NVE simulation is equivalent to an NPT at the equilibrated P and T from the NVE ensemble. One could also think that a NVE simulation is all what one needs to simulate any thermodynamic point,⁶⁷ however, practical simulated systems are usually too small for this to happen, and even in the case when they are big enough, it can be complicated to find out which energy value E is the correct one to simulate the desired thermodynamic point.^{68,69} This issue becomes more important for unknown materials produced at the interfaces for which we do not know their density neither their morphology and therefore their volume, thus, the NPT ensemble is justified for production runs because it allows us to obtain a suitable volume and energy rather than guessing them.^{66,70,71} In another study, Verners et al.⁷² performed MD simulations using the canonical NVT ensemble for the production runs to calculate ion diffusivity.

To calculate the voltage in the nanobattery, it requires to calculate the chemical potentials, which include the effects of entropy, which is not explicitly included; however, pressure is implicit in the calculations. The no inclusion of entropy is justified in this type of solids as entropy contribution to the chemical potentials is minimum based on a large amount of reports in the literature that do

not use it for solids. None of materials used in this work classify as high entropy alloys or so, where a consideration of entropy would be needed. Certainly, there are several other factors, perhaps of stronger effects than entropy that we understand are not included and that could have a larger contribution. For instance, the static effects of the electrons are included only as classical effects fitted into the force fields, but the dynamical component and parts of other quantum mechanical effects are not.

The energy difference $\Delta E = E_{\text{cathode}} - E_{\text{anode}} = -3.86 \text{ eV}$ without any external electric field (blue curve in Figure 5) yields the open-circuit voltage (OCV = 3.86 V) of this nanobattery, which is consistent with most of the commercial Li-ion batteries voltages ranging from 3 to 4.1 V. During discharge, the battery should spontaneously yield a discharging external current of electrons from the anode to the cathode as soon as a load (resistance) is connected to the two electrodes; simultaneously and internally, Li-ions travel from anode to cathode (same directions as electrons). To charge this battery (red curve in Figure 5), we need to apply an external field to at least counteract the OCV plus an additional potential to regulate the amount of current. Based on our previous work, we estimated that an external electric field of $\mathcal{E} = 0.75 \text{ V/\AA}$ would be enough to charge nanobatteries in an “acceptable” computational time. It is also important to mention that our computational setup before the application of the external field corresponds to open-circuit conditions, i.e., while the external bias or external device is not externally connected to the nanobattery electrodes. Therefore, no electrons (externally) and no ions (internally) can transfer between electrodes. Also Li-ions cannot penetrate the cathode in an open-circuit condition; they can only penetrate the cathode when the circuit is closed externally with a passive device (e.g., a resistor), i.e., during the discharge of the battery.

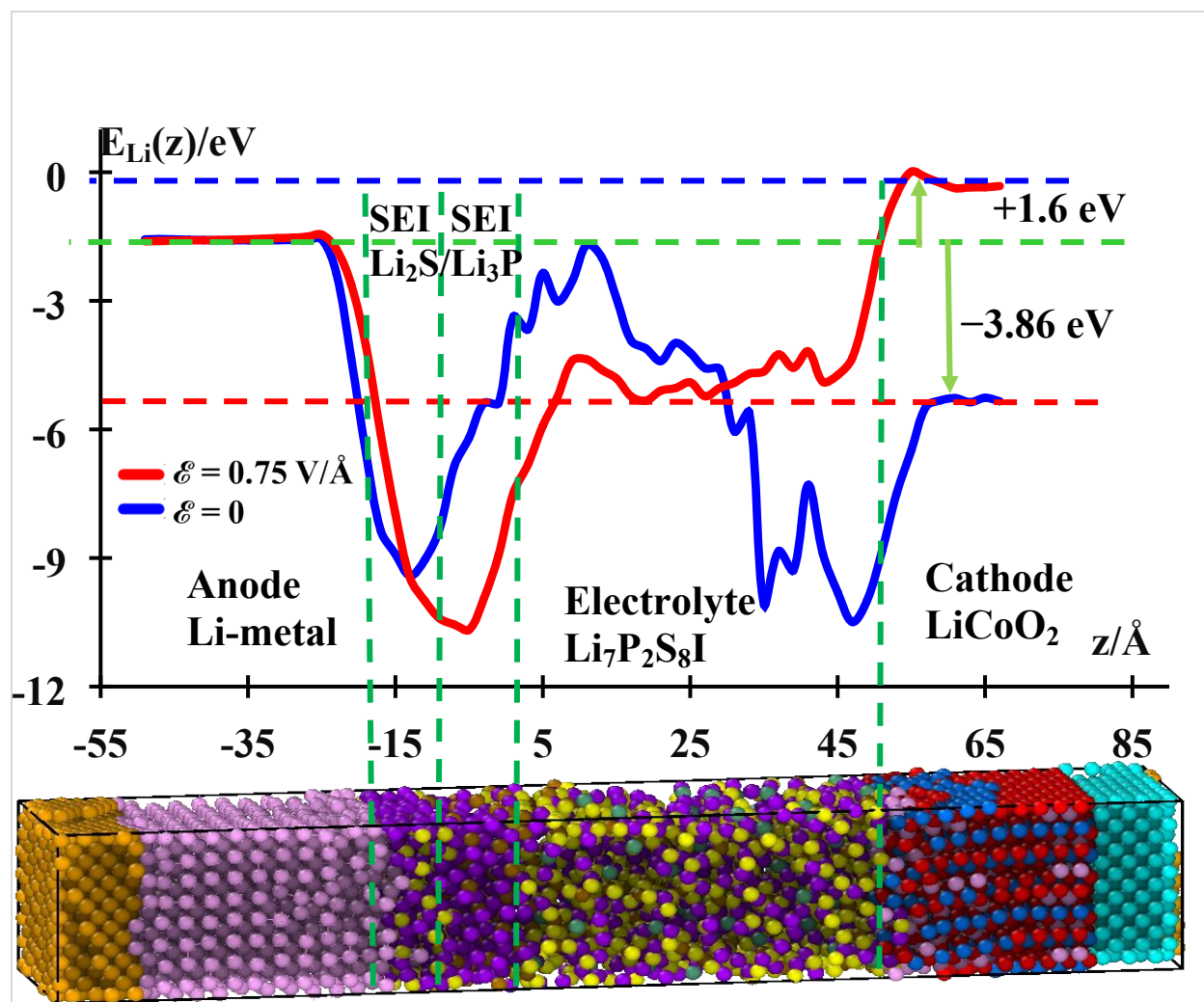


Figure 5. Li^+ potential energy profile along the longitudinal z -axis of the SSE calculated using a 12 \AA radius cutoff during the MD simulations without electric field $\mathcal{E} = 0$ (blue) and with electric field, $\mathcal{E} = 0.75 \text{ V/\AA}$ (red). Both calculations were performed at 300K under NPT ensembles and the frames to calculate potentials were taken every 100 fs.

In these conditions, the electric field yielded a potential energy of the cathode larger by 1.6 eV than the anode potential. This yields a charging voltage of 5.46 V. The additional 1.6 V is actually too high, in practical terms, to charge a real battery because other unwanted reactions could be activated at this large charging potentials, such as poor plating or dendrites growth in the anode or the cathode becoming an oxidizing agent, losing its stability releasing oxygen and producing CO_2 .⁷³ Certainly, at this point of high pressure, the cell eventually might vent with flame. Thus, in the simulations, a high charging voltage is used with the sole purpose of accelerating the calculations and inducing a faster cationic transport from cathode to anode. There is a potential drop at the cathode/SSE and SSE/SEI interfaces, and an uphill energetic profile is detected to move the ion through the SEI. Therefore, a technological value is found for $\text{Li}_7\text{P}_2\text{S}_8\text{I}$ as SSE as it can be expected to yield a dendrite-free anode, as well as a profound computational importance as we are able to predict the working voltage of the battery from the atomistic nature of its components.

Li^+ drifts through the two films of SEI, Li_3P and Li_2S , by a hopping mechanism, where Li^+ drifts by into a vacancy, similar to the Li^+ diffusion in $\text{Li}_7\text{P}_2\text{S}_8\text{I}^{30}$ and $\text{Li}_{10}\text{GeP}_2\text{S}_{12}^{31}$ solid state electrolytes. In this process, Li^+ hops one inter-atomic distance and remains until a vacancy appears adjacent to the Li^+ location, then Li^+ hops into the vacancy; the vacancy moves away and the process repeats, also partially resembling a knock-off mechanism, especially in the films, as vacancies are also created by the action of the electric field, yielding atomic reorganizations (Figure 6). Li^+ drifts nearby S in the SSE and Li_2S , compensating coulombic forces, and correspondingly, nearby P in Li_3P , forming ionic bonds at $\sim 2.4 \text{ \AA}$.

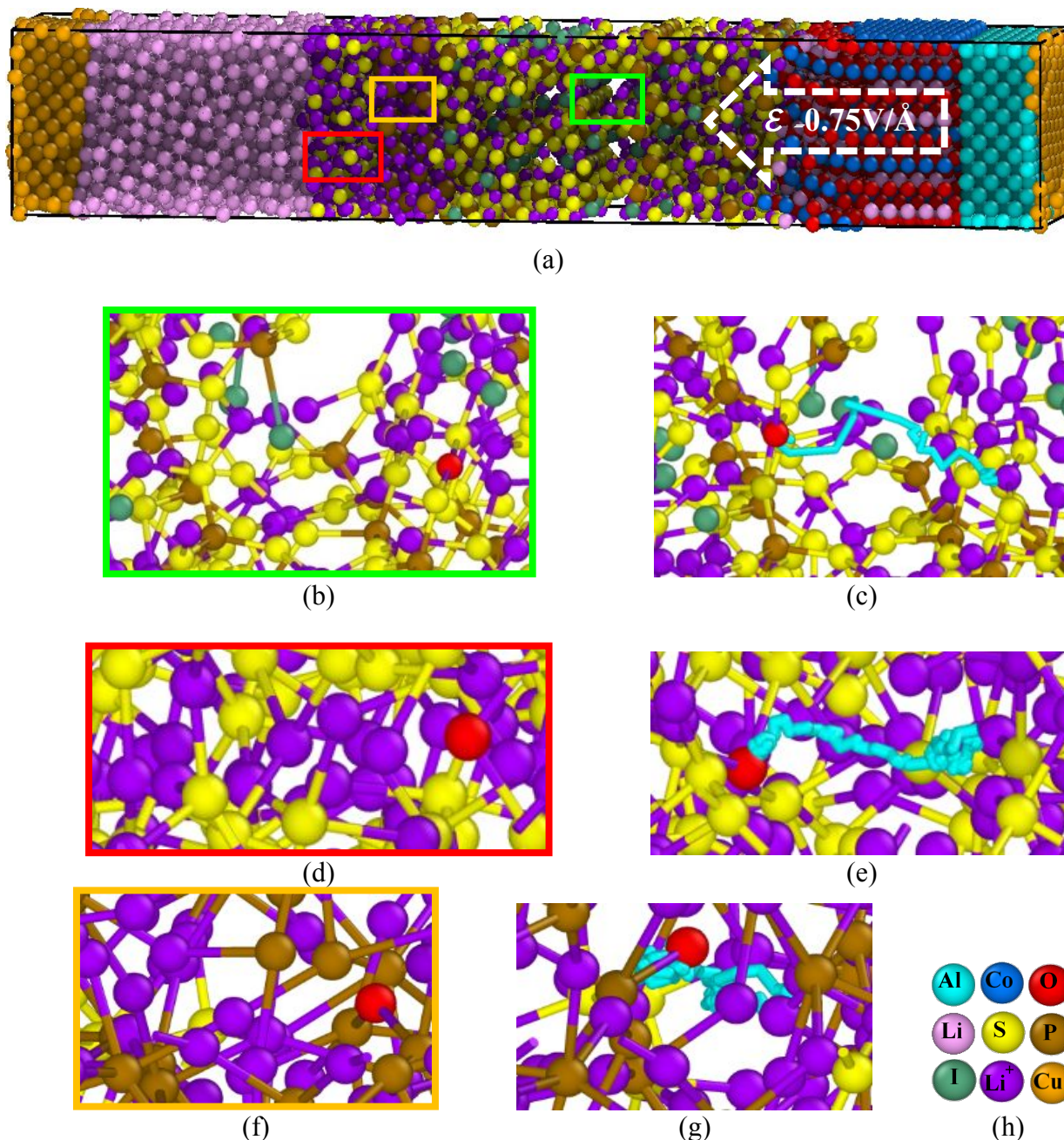


Figure 6. (a) Full nanobattery showing three initial regions (color rectangles) under study at the time of applying the electric field, $t = 0 \text{ ps}$. (b, d, f) Corresponding close ups of the three initial regions (at $t = 0$ of

the application of the electric field) from the nanobattery, showing one selected Li-ion (red) in each color box and eliminating frontal atoms that might cloud visibility. (c, e, g) Final positions corresponding to the initial positions b, d, and f, respectively, at $t = 3.2$ ps, under the external electric field of $\mathcal{E} = 0.75$ V/Å, showing also the Li-ion trajectory (light blue) during the 3.2 ps. LiPSI SSE (green boxes), Li₃P SEI (yellow boxes) and Li₂S SEI (red boxes). (h) Color code for atoms. Notice that oxygens (red) only appear in panel a. Panels b-g show the Li⁺ under study in red color.

CONCLUSIONS

We have developed a very useful model of a nano-version of a solid-state battery with a lithium-metal anode. This specific model included a double layer film acting as an artificial solid electrolyte interface, allowing us to study the behavior of interfaces on the anode-electrolyte side. We determine the thermal, speciation, and electrical features of the nanobattery before and after the application of an external field, simulating the charging cycle of a battery. Results were very encouraging as we were able to determine the open-circuit voltage of the nanobattery of 3.86 V, which is in very good agreement with commercial Li-ion based batteries. We also were able to determine the corresponding charging voltage generated by the applied external electrical field. As far as we understand, this type of calculation has not been done before using atomistic approaches. It was determined that the external field of $\mathcal{E} = 0.75$ V/Å yielded an external applied voltage of 5.46 V. It was also determined that before the external field is applied, a small temperature rise was located at the SEI (~315K) due to the reactions taking place there; besides, P S₃⁻ and P₂S₇⁴⁻ species are formed at the interfaces lithium-metal/SEI and SEI/SSE from the PS₃⁻ and PS₃I²⁻ anions under the presence of the external electric field. Li⁺ drift through the two films of the SEI, Li₃P and Li₂S by a hopping mechanism; the Li⁺ transport paths through the SSE and Li₃P film is through the vacancies and making ionic bonds of ~2.4 Å with P or S and supported by vacancies driven by the action of the electric field towards the surface of the films.

Basically, what this work tells us is about the possible use of protective films as layers of artificial SEI to cover and protect Li-metal anodes. This allows us to eliminate dendrites and also to have a more stable anode surface as well as acceptable Li-ion diffusion. Another important application are the maps of temperatures as we are able to determine the hot spots, perhaps dangerous, in the battery. Another is the speciation taking place at the interfaces. These are of strong importance for the experimentalists and battery builders. Definitely, our findings provide information to experimentalists to use new materials with calculated improved properties and the best way to exploit these results is to establish collaborations with experimental groups involved in the use of SSE using Li-metal anodes. A theoretical-guided approach to the design of new materials for batteries would be the best way to exploit these techniques.

CONFLICTS OF INTEREST

There are no conflicts of interest to declare.

ACKNOWLEDGEMENTS

This work was supported by the Assistant Secretary for Energy Efficiency and Renewable Energy, Vehicle Technologies Office of the U.S. Department of Energy under Contract No. DE-EE0007766 under the Advanced Battery Materials Research (BMR) Program and Battery 500 Consortium Award Number DE-EE0008210. Supercomputer resources from Texas A&M University High Performance Computer Center and Texas Advanced Computing Center (TACC) are gratefully acknowledged.

REFERENCES

- 1 Thomas, J., *Solid State Electrochemistry*. 8 ed.; Cambridge University Press: Cambridge, 1996; p 344.
- 2 Arbabzadeh, M.; Sioshansi, R.; Johnson, J. X.; Keoleian, G. A., The Role of Energy Storage in Deep Decarbonization of Electricity Production. *Nat. Commun.*, 2019, **10**, 3413.
- 3 Liu, H.; Cheng, X.-B.; Huang, J.-Q.; Yuan, H.; Lu, Y.; Yan, C.; Zhu, G.-L.; Xu, R.; Zhao, C.-Z.; Hou, L.-P.; He, C.; Kaskel, S.; Zhang, Q., Controlling Dendrite Growth in Solid-State Electrolytes. *ACS Energy Letters*, 2020, **5**, 833-843.
- 4 Belviso, F.; Claerbout, V. E. P.; Comas-Vives, A.; Dalal, N. S.; Fan, F.-R.; Filippetti, A.; Fiorentini, V.; Foppa, L.; Franchini, C.; Geisler, B.; Ghiringhelli, L. M.; Groß, A.; Hu, S.; Íñiguez, J.; Kauwe, S. K.; Musfeldt, J. L.; Nicolini, P.; Pentcheva, R.; Polcar, T.; Ren, W.; Ricci, F.; Ricci, F.; Sen, H. S.; Skelton, J. M.; Sparks, T. D.; Stroppa, A.; Urru, A.; Vandichel, M.; Vavassori, P.; Wu, H.; Yang, K.; Zhao, H. J.; Puggioni, D.; Cortese, R.; Cammarata, A., Viewpoint: Atomic-Scale Design Protocols toward Energy, Electronic, Catalysis, and Sensing Applications. *Inorg. Chem.*, 2019, **58**, 14939-14980.
- 5 Jin, Y.; Liu, K.; Lang, J.; Jiang, X.; Zheng, Z.; Su, Q.; Huang, Z.; Long, Y.; Wang, C.-a.; Wu, H.; Cui, Y., High-Energy-Density Solid-Electrolyte-Based Liquid Li-S and Li-Se Batteries. *Joule*, 2020, **4**, 262-274.
- 6 Li, J.; Ma, C.; Chi, M.; Liang, C.; Dudney, N. J., Solid Electrolyte: The Key for High-Voltage Lithium Batteries. *Adv. Energy Mater.*, 2015, **5**, 1401408.
- 7 Hu, Y.-S., Batteries: Getting Solid. *Nature Energy*, 2016, **1**, 16042.
- 8 Ponce, V.; Galvez-Aranda, D. E.; Seminario, J. M., Analysis of a Li-Ion Nanobattery with Graphite Anode Using Molecular Dynamics Simulations. *J. Phys. Chem. C*, 2017, **121**, 12959-12971.
- 9 Galvez-Aranda, D. E.; Ponce, V.; Seminario, J. M., Molecular Dynamics Simulations of the First Charge of a Li-Ion—Si-Anode Nanobattery. *J. Mol. Model.*, 2017, **23**, 120.
- 10 Kumar, N.; Seminario, J. M., Lithium-Ion Model Behavior in an Ethylene Carbonate Electrolyte Using Molecular Dynamics. *J. Phys. Chem. C*, 2016, **120**, 16322-16332.
- 11 Benitez, L.; Seminario, J. M., Electron Transport and Electrolyte Reduction in the Solid-Electrolyte Interphase of Rechargeable Lithium Ion Batteries with Silicon Anodes. *J. Phys. Chem. C*, 2016, **120**, 17978-17988.
- 12 Selis, L. A.; Seminario, J. M., Dendrite Formation in Silicon Anodes of Lithium-Ion Batteries. *RSC Advances*, 2018, **8**, 5255-5267.
- 13 Selis, L. A.; Seminario, J. M., Dendrite Formation in Li-Metal Anodes: An Atomistic Molecular Dynamics Study. *RSC Advances*, 2019, **9**, 27835-27848.
- 14 Jha, S.; Ponce, V.; Seminario, J. M., Investigating the Effects of Vacancies on Self-Diffusion in Silicon Clusters Using Classical Molecular Dynamics. *J. Mol. Model.*, 2018, **24**, 290.
- 15 Galvez-Aranda, D. E.; Seminario, J. M., Simulations of a LiF Solid Electrolyte Interphase Cracking on Silicon Anodes Using Molecular Dynamics. *J. Electrochem. Soc.*, 2018, **165**, A717-A730.
- 16 Galvez-Aranda, D. E.; Seminario, J. M., Ab Initio Study of the Interface of the Solid-State Electrolyte $\text{Li}_9\text{N}_2\text{Cl}_3$ with a Li-Metal Electrode. *J. Electrochem. Soc.*, 2019, **166**, A2048-A2057.

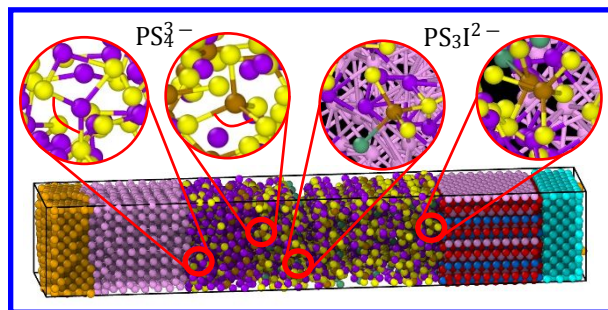
- 17 Ismail, I.; Noda, A.; Nishimoto, A.; Watanabe, M., XPS Study of Lithium Surface after Contact with Lithium-Salt Doped Polymer Electrolytes. *Electrochim. Acta*, 2001, **46**, 1595-1603.
- 18 Kanamura, K., Chemical Reaction of Lithium Surface During Immersion in LiClO₄ or LiPF₆/DEC Electrolyte. *J. Electrochem. Soc.*, 1997, **144**, 1900.
- 19 Kanamura, K., X-Ray Photoelectron Spectroscopic Analysis and Scanning Electron Microscopic Observation of the Lithium Surface Immersed in Nonaqueous Solvents. *J. Electrochem. Soc.*, 1994, **141**, 2379.
- 20 Kanamura, K.; Tamura, H.; Takehara, Z.-i., XPS Analysis of a Lithium Surface Immersed in Propylene Carbonate Solution Containing Various Salts. *J. Electroanal. Chem.*, 1992, **333**, 127-142.
- 21 Kanamura, K.; Tamura, H.; Shiraishi, S.; Takehara, Z.-I., XPS Analysis for the Lithium Surface Immersed in Γ -Butyrolactone Containing Various Salts. *Electrochim. Acta*, 1995, **40**, 913-921.
- 22 Kanamura, K., XPS Analysis of Lithium Surfaces Following Immersion in Various Solvents Containing LiBF₄. *J. Electrochem. Soc.*, 1995, **142**, 340.
- 23 Hong, S.-T.; Kim, J.-S.; Lim, S.-J.; Yoon, W. Y., Surface Characterization of Emulsified Lithium Powder Electrode. *Electrochim. Acta*, 2004, **50**, 535-539.
- 24 Shiraishi, S.; Kanamura, K.; Takehara, Z., Effect of Surface Modification Using Various Acids on Electrodeposition of Lithium. *J. Appl. Electrochem.*, 1995, **25**, 584-591.
- 25 Kamphaus, E. P.; Angarita-Gomez, S.; Qin, X.; Shao, M.; Engelhard, M.; Mueller, K. T.; Murugesan, V.; Balbuena, P. B., Role of Inorganic Surface Layer on Solid Electrolyte Interphase Evolution at Li-Metal Anodes. *ACS Appl. Mater. Interfaces*, 2019, **11**, 31467-31476.
- 26 Camacho-Forero, L. E.; Balbuena, P. B., Exploring Interfacial Stability of Solid-State Electrolytes at the Lithium-Metal Anode Surface. *J. Power Sources*, 2018, **396**, 782-790.
- 27 Liu, F.; Wang, L.; Zhang, Z.; Shi, P.; Feng, Y.; Yao, Y.; Ye, S.; Wang, H.; Wu, X.; Yu, Y., A Mixed Lithium-Ion Conductive Li₂S/Li₂Se Protection Layer for Stable Lithium Metal Anode. *Adv. Funct. Mater.*, 2020, **30**, 2001607.
- 28 Lin, L.; Liang, F.; Zhang, K.; Mao, H.; Yang, J.; Qian, Y., Lithium Phosphide/Lithium Chloride Coating on Lithium for Advanced Lithium Metal Anode. *J. Mater. Chem. A*, 2018, **6**, 15859-15867.
- 29 Yamamoto, T.; Phuc, N. H. H.; Muto, H.; Matsuda, A., Preparation of Li₇P₂S₈I Solid Electrolyte and Its Application in All-Solid-State Lithium-Ion Batteries with Graphite Anode. *Electron. Mater. Lett.*, 2019, **15**, 409-414.
- 30 Kang, J.; Han, B., First-Principles Characterization of the Unknown Crystal Structure and Ionic Conductivity of Li₇P₂S₈I as a Solid Electrolyte for High-Voltage Li Ion Batteries. *J. Phys. Chem. Lett.*, 2016, **7**, 2671-2675.
- 31 Mo, Y.; Ong, S. P.; Ceder, G., First Principles Study of the Li₁₀GeP₂S₁₂ Lithium Super Ionic Conductor Material. *Chem. Mater.*, 2012, **24**, 15-17.
- 32 Kato, Y.; Hori, S.; Saito, T.; Suzuki, K.; Hirayama, M.; Mitsui, A.; Yonemura, M.; Iba, H.; Kanno, R., High-Power All-Solid-State Batteries Using Sulfide Superionic Conductors. *Nat. Energy*, 2016, **1**, 16030.
- 33 Van Gunsteren, W. F.; Berendsen, H. J. C., A Leap-Frog Algorithm for Stochastic Dynamics. *Mol. Simul.*, 1988, **1**, 173-185.

- 34 Plimpton, S., Fast Parallel Algorithms for Short-Range Molecular Dynamics. *J. Comp. Phys.*, 1995, **117**, 1-19.
- 35 Spotnetz, R., Lithium-Ion Batteries. The Basics. *American Institute of Chemical Engineering CEP*, 2013, **October**, 39-43.
- 36 Humphrey, W.; Dalke, A.; Schulten, K., VMD: Visual Molecular Dynamics. *J. Mol. Graphics*, 1996, **14**, 33-38.
- 37 Alexander, S., Visualization and Analysis of Atomistic Simulation Data with OVITO—the Open Visualization Tool. *Modell. Simul. Mater. Sci. Eng.*, 2010, **18**, 015012.
- 38 Islam, M. M.; van Duin, A. C. T., Reductive Decomposition Reactions of Ethylene Carbonate by Explicit Electron Transfer from Lithium: An Ereaxff Molecular Dynamics Study. *J. Phys. Chem. C*, 2016, **120**, 27128-27134.
- 39 Becke, A. D., Density Functional Thermochemistry. III. The Role of Exact Exchange. *J. Chem. Phys.*, 1993, **98**, 5648-5652.
- 40 Perdew, J. P.; Burke, K.; Wang, Y., Generalized Gradient Approximation for the Exchange-Correlation Hole of a Many-Electron System. *Phys. Rev. B*, 1996, **54**, 16533-16539.
- 41 Perdew, J. P.; Chevary, J.; Vosko, S.; Jackson, K. A.; Pederson, M. R.; Singh, D.; Fiolhais, C., Atoms, Molecules, Solids, and Surfaces: Applications of the Generalized Gradient Approximation for Exchange and Correlation. *Phys. Rev. B*, 1992, **46**, 6671-6687.
- 42 Dunning, T. H., Gaussian Basis Sets for Use in Correlated Molecular Calculations. I. The Atoms Boron through Neon and Hydrogen. *J. Chem. Phys.*, 1989, **90**, 1007-1023.
- 43 Kendall, R. A.; Dunning, T. H.; Harrison, R. J., Electron Affinities of the First-Row Atoms Revisited. Systematic Basis Sets and Wave Functions. *J. Chem. Phys.*, 1992, **96**, 6796-6806.
- 44 Peterson, K. A.; Woon, D. E.; Dunning, T. H., Benchmark Calculations with Correlated Molecular Wave Functions. IV. The Classical Barrier Height of the $\text{H}+\text{H}_2\rightarrow\text{H}_2+\text{H}$ Reaction. *J. Chem. Phys.*, 1994, **100**, 7410-7415.
- 45 Dunning, T. H.; Hay, P. J., *Modern Theoretical Chemistry*. 3 ed.; Plenum Press: New York, 1977.
- 46 Hay, P. J.; Wadt, W. R., Ab Initio Effective Core Potentials for Molecular Calculations. Potentials for the Transition Metal Atoms Sc to Hg. *J. Chem. Phys.*, 1985, **82**, 270-283.
- 47 Wadt, W. R.; Hay, P. J., Ab Initio Effective Core Potentials for Molecular Calculations. Potentials for Main Group Elements Na to Bi. *J. Chem. Phys.*, 1985, **82**, 284-298.
- 48 Hay, P. J.; Wadt, W. R., Ab Initio Effective Core Potentials for Molecular Calculations. Potentials for K to Au Including the Outermost Core Orbitals. *J. Chem. Phys.*, 1985, **82**, 299-310.
- 49 Frisch, M. J.; Trucks, G. W.; Schlegel, H. B.; G. E. Scuseria; Robb, M. A.; Cheeseman, J. R.; Scalmani, G.; Barone, V.; Petersson, G. A.; Nakatsuji, H.; Li, X.; Caricato, M.; Marenich, A. V.; Bloino, J.; Janesko, B. G.; Gomperts, R.; Mennucci, B.; Hratchian, H. P.; Ortiz, J. V.; Izmaylov, A. F.; Sonnenberg, J. L.; D. Williams-Young; F. Ding, F. L.; Egidi, F.; Goings, J.; Peng, B.; Petrone, A.; Henderson, T.; Ranasinghe, D.; Zakrzewski, V. G.; J. Gao, N. R.; Zheng, G.; Liang, W.; Hada, M.; Ehara, M.; Toyota, K.; Fukuda, R.; Hasegawa, J.; Ishida, M.; Nakajima, T.; Honda, Y.; Kitao, O.; Nakai, H.; Vreven, T.; Throssell, K.; Montgomery, J. A., Jr.; J. E. P.; Ogliaro, F.; Bearpark, M. J.; Heyd, J. J.; Brothers, E. N.; Kudin, K. N.; Staroverov, V. N.; Keith, T. A.; Kobayashi, R.; Normand, J.; Raghavachari, K.; Rendell, A. P.; Burant, J. C.; Iyengar, S. S.; Tomasi, J.; Cossi, M.; Millam, J. M.; Klene, M.; Adamo, C.; Cammi, R.; Ochterski, J. W.; Martin, R. L.; Morokuma, K.; Farkas, O.; Foresman, J. B.; Fox, D. J. *Gaussian 16, Revision B.01*, Gaussian, Inc.: Wallingford CT, 2016.

- 50 Sumita, M.; Tanaka, Y.; Ohno, T., Possible Polymerization of PS_4 at a $\text{Li}_3\text{PS}_4/\text{FePO}_4$ Interface with Reduction of the FePO_4 Phase. *J. Phys. Chem. C*, 2017, **121**, 9698-9704.
- 51 Khoda, K. M.; Liu, Y.; Storey, C., Generalized Polak-Ribière Algorithm. *J. Optim. Theory Appl.*, 1992, **75**, 345-354.
- 52 Nauchitel, V. V., Energy-Distribution Function for the NVT Canonical Ensemble. *Mol. Phys.*, 1981, **42**, 1259-1265.
- 53 Kalibaeva, G.; Ferrario, M.; Ciccotti, G., Constant Pressure-Constant Temperature Molecular Dynamics: A Correct Constrained NPT Ensemble Using the Molecular Virial. *Mol. Phys.*, 2003, **101**, 765-778.
- 54 Nosé, S., A Molecular Dynamics Method for Simulations in the Canonical Ensemble. *Mol. Phys.*, 1984, **52**, 255-268.
- 55 Melchionna, S.; Ciccotti, G.; Lee Holian, B., Hoover NPT Dynamics for Systems Varying in Shape and Size. *Mol. Phys.*, 1993, **78**, 533-544.
- 56 Rangasamy, E.; Liu, Z.; Gobet, M.; Pilar, K.; Sahu, G.; Zhou, W.; Wu, H.; Greenbaum, S.; Liang, C., An Iodide-Based $\text{Li}_7\text{P}_2\text{S}_8\text{I}$ Superionic Conductor. *J. Am. Chem. Soc.*, 2015, **137**, 1384-1387.
- 57 Xie, J.; Imanishi, N.; Matsumura, T.; Hirano, A.; Takeda, Y.; Yamamoto, O., Orientation Dependence of Li-Ion Diffusion Kinetics in LiCoO_2 Thin Films Prepared by RF Magnetron Sputtering. *Solid State Ion.*, 2008, **179**, 362-370.
- 58 Dence, J. B., Heat Capacity and the Equipartition Theorem. *J. Chem. Educ.*, 1972, **49**, 798.
- 59 Khodel, V.; Clark, J.; Shaginyan, V. R.; Zverev, M., Second Wind of the Dulong-Petit Law at a Quantum Critical Point. *JETP letters*, 2010, **92**, 532-536.
- 60 Pickover, C., *Archimedes to Hawking: Laws of Science and the Great Minds Behind Them*. Oxford University Press: 2008.
- 61 Hicks, D. G.; Boehly, T. R.; Eggert, J. H.; Miller, J. E.; Celliers, P. M.; Collins, G. W., Dissociation of Liquid Silica at High Pressures and Temperatures. *Phys. Rev. Lett.*, 2006, **97**, 025502.
- 62 Naumovets, A.; Poluektov, Y.; Khodusev, V., Nonlinear Effects in the Phonon System of Diamond Crystal. *East Eur. J. Phys.*, 2003, **2**, 124-135.
- 63 Rekhviashvili, S. S.; Kunizhev, K. L., Investigation of the Influence of Lattice Anharmonicity on the Heat Capacities of Diamond, Silicon, and Germanium. *High Temp*, 2017, **55**, 312-314.
- 64 Rödl, T.; Wehrich, R.; Wack, J.; Senker, J.; Pfitzner, A., Rational Syntheses and Structural Characterization of Sulfur-Rich Phosphorus Polysulfides: $\alpha\text{-P}_2\text{S}_7$ and $\beta\text{-P}_2\text{S}_7$. *Angew. Chem. Int. Ed.*, 2011, **50**, 10996-11000.
- 65 Toxvaerd, S., Dynamics of Homogeneous Nucleation. *J. Chem. Phys.*, 2015, **143**, 154705.
- 66 Chalaris, M.; Samios, J., Systematic Molecular Dynamics Studies of Liquid N,N-Dimethylformamide Using Optimized Rigid Force Fields: Investigation of the Thermodynamic, Structural, Transport and Dynamic Properties. *J. Chem. Phys.*, 2000, **112**, 8581-8594.
- 67 Hammonds, K. D.; Heyes, D. M., Shadow Hamiltonian in Classical NVE Molecular Dynamics Simulations: A Path to Long Time Stability. *J. Chem. Phys.*, 2020, **152**, 024114.
- 68 Ellis, R. S.; Touchette, H.; Turkington, B., Thermodynamic Versus Statistical Nonequivalence of Ensembles for the Mean-Field Blume-Emery-Griffiths Model. *Physica A*, 2004, **335**, 518-538.
- 69 Touchette, H.; Ellis, R. S.; Turkington, B., An Introduction to the Thermodynamic and Macrostate Levels of Nonequivalent Ensembles. *Physica A*, 2004, **340**, 138-146.

- 70 Xu, Y.; Jiang, H., Self-Assembly of Supported Lipid Multi-Bilayers Investigated by Time-Resolved X-Ray Diffraction. *Biochim Biophys Acta Biomembr*, 2020, **1862**, 183437.
- 71 Ombrato, R.; Console, L.; Righino, B.; Indiveri, C.; Arduini, A.; De Rosa, M. C., Structure-Based Virtual Screening to Identify Novel Carnitine Acetyltransferase Activators. *J. Mol. Graph. Model.*, 2020, **100**, 107692.
- 72 Verners, O.; Duin, A. C. T. v.; Wagemaker, M.; Simone, A., Molecular Dynamics Modeling of Structural Battery Components. In *20th International Conference on Composite Materials*, Copenhagen, 19-24th July, 2015.
- 73 Ohsaki, T.; Kishi, T.; Kuboki, T.; Takami, N.; Shimura, N.; Sato, Y.; Sekino, M.; Satoh, A., Overcharge Reaction of Lithium-Ion Batteries. *J. Power Sources*, 2005, **146**, 97-100.

TOC



The full nanobattery showing speciations at SEI and SSE.